

Few-shot Object Counting with Similarity-Aware Feature Enhancement

Zhiyuan You¹ Yujun Shen² Kai Yang³ Wenhan Luo⁴
Xin Lu³ Lei Cui³ Xinyi Le¹

¹Shanghai Jiao Tong University ²CUHK ³Sensetime ⁴Tencent

Abstract. This work studies the problem of few-shot object counting, which counts the number of exemplar objects (*i.e.*, described by one or several support images) occurring in the query image. The major challenge lies in that the target objects can be densely packed in the query image, making it hard to recognize every single one. To tackle the obstacle, we propose a novel learning block, equipped with a similarity comparison module (SCM) and a feature enhancement module (FEM). Concretely, given a support image and a query image, we first derive a score map by comparing their projected features at every spatial position. The score maps regarding all support images are collected together and normalized across both the exemplar dimension and the spatial dimensions, producing a reliable similarity map. We then enhance the query feature with the support features by employing the developed point-wise similarities as the weighting coefficients. Such a design encourages the model to inspect the query image by *focusing more on the regions akin to the support images, leading to much clearer boundaries between different objects*. Extensive experiments on various benchmarks and training setups suggest that our method surpasses the state-of-the-art approaches by a sufficiently large margin. For instance, on the very recent large-scale FSC-147 dataset, we beat the second competitor by improving the mean absolute counting error from 22.08 to 14.32 (35% \uparrow).

1 Introduction

Object counting [3, 4], which aims at investigating how many times a certain object occurs in the query image, has received growing attention due to its practical usage [9, 15, 22, 51]. Most existing studies assume that the object to count at the test stage is covered by the training data [1, 12, 22, 33, 50, 51]. As a result, each learned model can only handle a specific object class, greatly limiting its application.

To alleviate the generalization problem, few-shot object counting (FSC) is recently introduced [26]. Instead of pre-defining a common object that is shared by all training images, FSC allows users to customize the object of their own interests with a few support images, as shown in Fig. 1. In this way, we can use a single model to unify the counting of various objects very efficiently, and even adapt the model to novel classes (*i.e.*, unseen in the training phase) without any retraining.

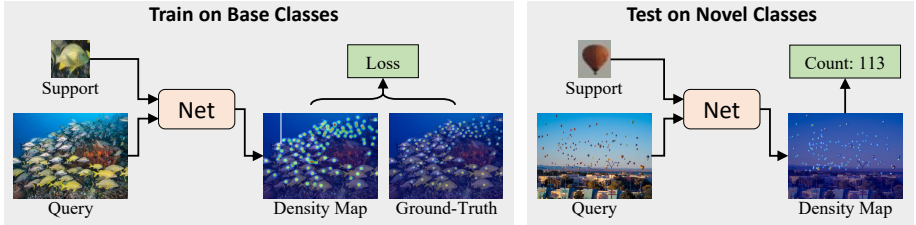


Fig. 1. Illustration of few-shot object counting, where we would like to find how many exemplar objects described by *a few* support images occur in the query image. Besides the objects included in the training phase, we also expect the model to handle novel classes at the test stage without retraining

A popular solution to FSC is to first represent both the exemplar object (*i.e.* the support image) and the query image with expressive features, and then pinpoint the candidates via analyzing the feature correlation [23, 26, 46]. Active attempts roughly fall into two folds. One is feature-based [23], as shown in Fig. 2a, where the pooled support feature is concatenated onto the query feature, followed by a regress head to recognize whether the two features are close enough. However, the spatial information of the support image is omitted by pooling, leaving the feature comparison unreliable. The other is similarity-based [26, 46], as shown in Fig. 2b, where a similarity map is developed from raw features as the regression object. Nevertheless, the similarity is far less informative than feature, making it hard to identify clear boundaries between objects (see Fig. 5). Accordingly, the counting performance heavily deteriorates when the target objects are densely packed in the query image, like the shoal of fish in Fig. 1.

In this work, we propose a similarity-aware feature enhancement block for object counting, shortened to SAFECOUNT. As discussed above, *feature is more informative while similarity better captures the support-query relationship*. Our novel block adequately integrates both of the advantages by exploiting similarity as a guidance to enhance the features for regression. Intuitively, the enhanced feature not only carries the rich semantics extracted from the image, but also gets aware of which regions within the query image are similar to the exemplar object. Specifically, we come up with a similarity comparison module (SCM) and a feature enhancement module (FEM), as illustrated in Fig. 2c. On one hand, different from the naive feature comparison in Fig. 2b, our SCM learns a feature projection, then performs a comparison on the projected features to derive a score map. This design helps select from features the information that is most appropriate for object counting. After the comparison, we derive a reliable similarity map by collecting the score maps with respect to all support images (*i.e.*, few-shot) and normalizing them along both the exemplar dimension and the spatial dimensions. On the other hand, the FEM takes the point-wise similarities as the weighting coefficients, and fuses the support features into the query feature. Such a fusion is able to make the enhanced query feature focus more on the regions akin to the exemplar object defined by support images, facilitating more precise counting.

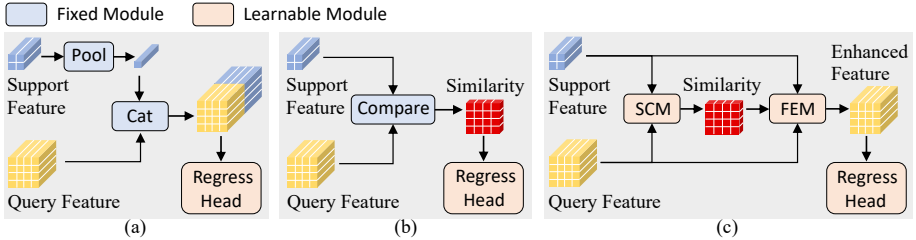


Fig. 2. Concept comparison between our method and existing alternatives. (a) Feature-based approach [23], where the query feature is concatenated with the pooled support feature for regression. (b) Similarity-based approach [26, 46], where a similarity map is developed from raw features for regression. (c) Our proposed *similarity-aware feature enhancement* block, consisting of a similarity comparison module (SCM) and a feature enhancement module (FEM). Concretely, the reliable feature similarity developed by SCM is exploited as the guidance of FEM to enhance the query feature with the support feature. The details of SCM and FEM can be found in Sec. 3.2 and Fig. 3

Experimental results on a range of benchmarks, including FSC-147 [26], CARPK [12], PUCPR+ [12], UCSD [3], Mall [4], and ShanghaiTech [51], demonstrate our *sufficient superiority* over state-of-the-art methods. Through visualizing the intermediate similarity map and the final predicted density map, we find that our SAFECOUNT substantially benefits from the clear boundaries learned between objects, even when they are densely packed in the query image.

2 Related Work

Class-specific object counting counts objects of a specific class, such as people [22, 33, 50, 51], animals [1], cars [12], among which crowd counting has been widely explored. For this purpose, traditional methods [16, 35, 39] count the number of people occurring in an image through person detection. However, object detection is not particularly designed for the counting task and hence shows unsatisfying performance when the crowd is thick. To address this issue, recent work [38] employs a deep model to predict the density map from the crowd image, where the sum over the density map gives the counting result [17]. Based on this thought, many attempts have been made to handle more complicated cases [2, 21, 25, 29–31, 43, 44, 47, 49, 51]. Some recent studies [33, 37] propose effective loss functions that help predict the position of each person precisely. However, all of these methods can only count objects regarding a particular class (*e.g.*, person), making them hard to generalize. There are also some approaches targeting counting objects of multiple classes [9, 15, 34]. In particular, Stahl *et al.* [34] propose to divide the query image into regions and regress the counting results with the inclusion-exclusion principle. Goldman *et al.* [9] improve counting performance with Soft-IOU and EM-Merger. Laradji *et al.* [15] formulate counting as a segmentation problem for better localization. Nevertheless, they still can not handle the object classes beyond the training data.

Few-shot object counting (FSC) has recently been proposed [23, 26, 46] and presents a much stronger generalization ability. Instead of pre-knowing the type of object to count, FSC allows users to describe the exemplar object of their own interests with *one or several* support images. This setting makes the model highly flexible in that it does not require the test object to be covered by the training samples. In other words, a well-learned model could easily make inferences on novel classes (*i.e.*, unseen in the training phase) as long as the support images are provided. To help the model dynamically get adapted to an arbitrary class, a great choice is to compare the object and the query image in feature space [23, 26, 46]. GMN [23] pools the support feature, and concatenates the pooling result onto the query feature, then learns a regression head for point-wise feature comparison. However, the comparison built on concatenation is not as reliable as the similarity [46]. Instead, CFOCNet [46] first performs feature comparison with dot production, and then regresses the density map from the similarity map derived before. FamNet [26] further improves the reliability of the similarity map through multi-scale augmentation and test-time adaptation. But similarities are far less informative than features, hence regressing from the similarity map fails to identify clear boundaries between the densely packed objects. In this work, we propose a similarity-aware feature enhancement block, which integrates the advantages of both features and similarities.

Few-shot learning has received popular attention in the past few years thanks to its high data efficiency [6, 8, 41, 42, 45, 48]. The rationale behind this is to adapt a well-trained model to novel test data (*i.e.*, having a domain gap to the training data) with a few support samples. In the field of image classification [8, 41], MAML [8] proposes to fit parameters to novel classes at the test stage using a few steps of gradient descent. FRN [41] formulates few-shot classification as a reconstruction problem. As for object detection [6, 42], Fan *et al.* [6] exploit the similarity between the input image and the support images to detect novel objects. Wu *et al.* [42] create multi-scale positive samples as the object pyramid for prediction refinement. When the case comes to semantic segmentation [45, 48], CANet [48] iteratively refines the segmentation results by comparing the query feature and the support feature. Yang *et al.* [45] aim to alleviate the problem of feature undermining and enhance the embedding of novel classes. In this work, we explore the usage of few-shot learning on the object counting task.

3 Method

3.1 Preliminaries

Few-shot object counting (FSC) [26] aims to count the number of exemplar objects occurring in a query image with only a few support images describing the exemplar object. In FSC, object classes are divided into base classes \mathcal{C}_b and novel classes \mathcal{C}_n , where \mathcal{C}_b and \mathcal{C}_n have no intersection. For each query image from \mathcal{C}_b , both a few support images and the ground-truth density map are provided. While, for query images from \mathcal{C}_n , only a few support images are available. FSC

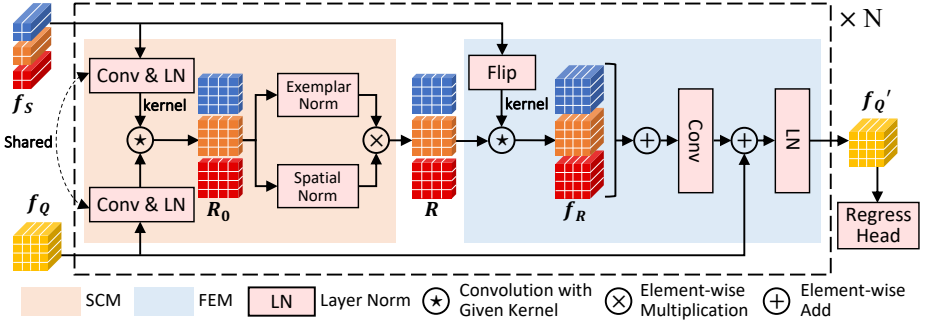


Fig. 3. Illustration of the similarity-aware feature enhancement block under the 3-shot case. Given features, f_S , f_Q , that are extracted from the support images and the query image respectively, the similarity comparison module (SCM) first develops a score map, R_0 , by comparing the projected features, and then produces a similarity map, R , via normalizing R_0 along both the exemplar dimension and the spatial dimensions. Here, feature projection is implemented with a 1×1 convolution. The following feature enhancement module (FEM) weights f_S with R to derive a similarity-weighted feature, f_R , and manages to fuse f_R into f_Q as a feature enhancement. Such a block can be stacked for multiple times in the training framework

aims to count exemplar objects from C_n using only a few support images by leveraging the generalization knowledge from C_b . Denote the number of support images for a query image as K , the task is called K -shot FSC.

3.2 Similarity-Aware Feature Enhancement

Overview. Fig. 3 illustrates the core block in our framework, termed as the *similarity-aware feature enhancement* block. We respectively denote the support feature and the query feature as $f_S \in \mathbb{R}^{K \times C \times H_S \times W_S}$ and $f_Q \in \mathbb{R}^{C \times H_Q \times W_Q}$, where K is the number of support images. The similarity comparison module (SCM) first projects f_S and f_Q to a comparison space, then compares these projected features at every spatial position, deriving a score map, R_0 . Then, R_0 is normalized along both the exemplar dimension and the spatial dimensions, resulting in a reliable similarity map, R . The following feature enhancement module (FEM) first obtains the similarity-weighted feature, f_R , by weighting f_S with R , and then manages to fuse f_R into f_Q , producing the enhanced feature, f_Q' . By doing so, the features regarding the regions similar to the support images are “highlighted”, which could help the model get distinguishable borders between densely packed objects. Finally, the density map is regressed from f_Q' .

Similarity Comparison Module (SCM). As discussed above, similarity can better characterize how a particular image region is alike the exemplar object. However, we find that the conventional feature comparison approach (*i.e.*, using the vanilla dot production) used in prior arts [26, 46] is not adapted to fit the FSC task. By contrast, our proposed SCM develops a reliable similarity map from the input features with the following three steps.

Step-1: Learnable Feature Projection. Before performing feature comparison, \mathbf{f}_S and \mathbf{f}_Q are first projected to a comparison space via a 1×1 convolutional layer. This projection asks the model to automatically select suitable information from the features. We also add a shared layer normalization after the projection to make these two features subject to the same distribution as much as possible.

Step-2: Feature Comparison. The point-wise feature comparison is realized with convolution. In particular, we convolve the projected \mathbf{f}_Q with the projected \mathbf{f}_S as kernels, which gives us the score map,

$$\mathbf{R}_0 = \text{conv}(g(\mathbf{f}_Q), \text{kernel} = g(\mathbf{f}_S)) \in \mathbb{R}^{K \times 1 \times H_Q \times W_Q}, \quad (1)$$

where $g(\cdot)$ denotes the feature projection described in *Step-1*, i.e., a 1×1 convolutional layer followed layer normalization.

Step-3: Score Normalization. The values of the score map, \mathbf{R}_0 , are normalized to a proper range to avoid some unusual (e.g., too large) entries from dominating the learning. Here, we propose Exemplar Normalization (ENorm) and Spatial Normalization (SNorm). On the one hand, ENorm normalizes \mathbf{R}_0 along the exemplar dimension as

$$\mathbf{R}_{EN} = \text{softmax}\left(\frac{\mathbf{R}_0}{\sqrt{H_S W_S C}}, \dim = 0\right) \in \mathbb{R}^{K \times 1 \times H_Q \times W_Q}, \quad (2)$$

where $\text{softmax}(\cdot, \dim)$ is the softmax layer operated along a specific dimension. On the other hand, \mathbf{R}_0 is also normalized along the spatial dimensions (i.e., the height and width) with SNorm, as

$$\mathbf{R}_{SN} = \frac{\exp(\mathbf{R}_0 / \sqrt{H_S W_S C})}{\max(\exp(\mathbf{R}_0 / \sqrt{H_S W_S C}), \dim = (2, 3))} \in \mathbb{R}^{K \times 1 \times H_Q \times W_Q}, \quad (3)$$

where $\max(\cdot, \dim)$ finds the maximum value from the given dimensions. After SNorm, the score value of the most support-relevant position would be 1, and others would be among $[0, 1]$. Finally, the similarity map, \mathbf{R} , is obtained from \mathbf{R}_{EN} and \mathbf{R}_{SN} with

$$\mathbf{R} = \mathbf{R}_{EN} \otimes \mathbf{R}_{SN} \in \mathbb{R}^{K \times 1 \times H_Q \times W_Q}, \quad (4)$$

where \otimes stands for the element-wise multiplication. The studies of the effect of ENorm and SNorm can be found in Sec. 4.4.

Feature Enhancement Module (FEM). Recall that, compared to similarity, feature is more informative in representing the image yet less accurate in capturing the support-query relationship. To take sufficient advantages of both, we propose to use the similarity developed by SCM as the guidance for feature enhancement. Specifically, our FEM integrates the support feature, \mathbf{f}_S , into the query feature, \mathbf{f}_Q , with similarity values in \mathbf{R} as the weighting coefficients. In this way, the model can inspect the query image by paying more attention to the regions that are akin to the support images. Generally, this module consists of the following two steps.

Step-1: Weighted Feature Aggregation. In this step, we aggregate the support feature, \mathbf{f}_S , by taking the point-wise similarity, \mathbf{R} , into account. Namely, the feature point corresponding to a higher similarity score should have larger voice to the final enhancement. Such a weighted aggregation is implemented with convolution, which outputs the similarity-weighted feature,

$$\mathbf{f}'_R = \text{conv}(\mathbf{R}, \text{kernel} = \text{flip}(\mathbf{f}_S)) \in \mathbb{R}^{K \times C \times H_Q \times W_Q}, \quad (5)$$

$$\mathbf{f}_R = \text{sum}(\mathbf{f}'_R, \text{dim} = 0) \in \mathbb{R}^{C \times H_Q \times W_Q}, \quad (6)$$

where $\text{sum}(\cdot, \text{dim})$ accumulates the input tensor along specific dimensions, $\text{flip}(\cdot)$ denotes the flipping operation, which flips the input tensor both horizontally and vertically. Flipping helps \mathbf{f}'_R preserve the spatial structure of \mathbf{f}_S . The intuitive illustration and the performance improvement of flipping can be found in Appendix B.

Step-2: Learnable Feature Fusion. The similarity-weighted feature, \mathbf{f}_R , is fused into the query feature, \mathbf{f}_Q , via an efficient network. It contains a convolutional block and a layer normalization, as shown in Fig. 3. Finally, we obtain the enhanced feature, \mathbf{f}'_Q , with

$$\mathbf{f}'_Q = \text{layer_norm}(\mathbf{f}_Q + h(\mathbf{f}_R)) \in \mathbb{R}^{C \times H_Q \times W_Q}, \quad (7)$$

where $h(\cdot)$ is implemented with two convolutional layers.

3.3 Training Framework

Sec. 3.2 describes the core block of our approach, SAFECount. In practice, such a block should work together with a feature extractor, which feeds input features into the block, and a regression head, which receives the enhanced feature for object counting. Moreover, it is worth mentioning that our SAFECount allows stacking itself for continuous performance improvement. In this part, we will introduce these assistant modules, whose detailed structures are included in Appendix A.

Feature Extractor. When introducing our SAFECount block, we start with the support feature, \mathbf{f}_S , and the query feature, \mathbf{f}_Q , which are assumed to be well prepared. Virtually, we use a *fixed* ResNet-18 [11] pre-trained on ImageNet [5] as the feature extractor. In particular, given a query image, we resize the outputs of the first three residual stages of ResNet-18 to the same size, $H_Q \times W_Q$, and concatenate them along the channel dimension as the query feature. Besides, given a support image, which is usually cropped from a large image so as to contain the exemplar object only, the support feature is obtained by applying ROI pooling [28] on the feature extracted from its parent before cropping. Here, the ROI pooling size is set the same as \mathbf{f}_S , i.e., $H_S \times W_S$.

Regression Head. After getting the enhanced feature, \mathbf{f}'_Q , we convert it to a density map, $\mathbf{D} \in \mathbb{R}^{H \times W}$, with a regression head. Following existing methods [23, 26, 46], the regression head is implemented with a sequence of convolutional layers, followed by Leaky ReLU activation and bi-linear upsampling.

Multi-block Architecture. Recall that our proposed SAFECOUNT block enhances the input query feature, \mathbf{f}_Q , with the support features, \mathbf{f}_S . The enhanced feature, \mathbf{f}'_Q , is with exactly the same shape as \mathbf{f}_Q . As a result, it can be iteratively enhanced simply by stacking more blocks. The ablation study on the number of blocks can be found in Sec. 4.4, where we verify that *adding one block is already enough to boost the performance substantially*.

Objective Function. Most counting datasets are annotated with the coordinates of the target objects within the query image [3, 4, 51]. However, directly regressing the coordinates can be hard [17, 51]. Following prior work [26], we generate the ground-truth density map, $\mathbf{D}_{GT} \in \mathbb{R}^{H \times W}$, from the labeled coordinates, using Gaussian smoothing with adaptive window size. Then, our model is trained with the MSE loss as

$$\mathcal{L} = \frac{1}{H \times W} \|\mathbf{D} - \mathbf{D}_{GT}\|_2^2. \quad (8)$$

4 Experiments

4.1 Metrics and Datasets

Metrics. We choose Mean Absolute Error (MAE) and Root Mean Squared Error (RMSE) to measure the performance of counting methods following [9, 26]:

$$MAE = \frac{1}{N_Q} \sum_{i=1}^{N_Q} |C^i - C_{GT}^i|, \quad RMSE = \sqrt{\frac{1}{N_Q} \sum_{i=1}^{N_Q} (C^i - C_{GT}^i)^2}, \quad (9)$$

where N_Q is the number of query images, C^i and C_{GT}^i are the predicted and ground-truth count of the i^{th} query image, respectively.

FSC-147. FSC-147 [26] is a multi-class, 3-shot FSC dataset with 147 classes and 6135 images. Each image has 3 support images to describe the target objects. Note that the training classes share no intersection with the validation classes and test classes. The training set contains 89 classes, while validation set and test set both contain another disjoint 29 classes. The number of objects per image varies extremely from 7 to 3701 with an average of 56. In addition, the images collected from COCO [20] in validation set and test set of FSC-147 are named as Val-COCO and Test-COCO, which comprise of 277 and 282 images, respectively. These two subsets collected from COCO are also used as FSC evaluation datasets, especially for the comparison with detection-based approaches since COCO is a widely adopted detection benchmark.

Cross-validation of FSC-147. In the original FSC-147 [26], the dataset split and the shot number are both fixed, while other few-shot tasks including classification [41], detection [6], and segmentation [45] all contain multiple dataset splits and shot numbers. Therefore, we propose to evaluate FSC methods with multiple dataset splits and shot numbers by incorporating FSC-147 and cross-validation. Specifically, we split all images in FSC-147 to 4 folds, whose class

Table 1. Statistical information of the four different fold splits from FSC-147 dataset [26]

Fold	Class Indices	#Classes	#Images
0	0-35	36	2033
1	36-72	37	1761
2	73-109	37	1239
3	110-146	37	1113

Table 2. Class-specific counting datasets

Type	Dataset	#Images	#Objects
Car	CARPK [12]	1448	89,777
	PUCPR+ [12]	125	16,916
Crowd	PartA [51]	482	241,677
	PartB [51]	716	88,488
	UCSD [3]	2000	49,885
	Mall [4]	2000	62,325

indices, class number, and image number are shown in Tab. 1. The class indices ranging from 0 to 146 are obtained by sorting the class names of all 147 classes. Note that these 4 folds share no common classes. When fold- i ($i = 0, 1, 2, 3$) serves as the test set, the remaining 3 folds form the training set. Also, we evaluate FSC methods in both 1-shot and 3-shot cases. For 3-shot case, the original three support images in FSC-147 are used. For 1-shot case, we randomly sample one from the original three support images.

Class-specific Counting Datasets. Our method is designed to be a general class-agnostic FSC approach. Nonetheless, we still evaluate our method on class-specific counting tasks including two car counting datasets: CARPK [12] and PUCPR+ [12] and three crowd counting datasets: ShanghaiTech (PartA and PartB) [51], UCSD [3], and Mall [4] to further testify its superiority. The details of these datasets are given in Tab. 2.

4.2 Class-agnostic Few-shot Object Counting

The class-agnostic FSC performance of our method is evaluated on the FSC dataset FSC-147 [26] under the original setting and the cross-validation setting.

Setup. The sizes of the query image, the query feature map, and the support feature map, $H \times W$, $H_Q \times W_Q$, and $H_S \times W_S$, are selected as 512×512 , 128×128 , and 3×3 , respectively. The dimension of the projected features are set as 256. The multi-block number is set as 4. The model is trained with Adam optimizer [14] for 200 epochs with batch size 8. The learning rate is set as $2e-5$ initially, and it is dropped by 0.25 every 80 epochs.

FSC-147. Quantitative results on FSC-147 are given in Tab. 3a. Our approach is compared with baselines employed in [26]: FR few-shot detector [13], FSOD few-shot detector [7], GMN [23], MAML [8], and FamNet [26]. Our approach outperforms all counterparts with a quite large margin. For example, our method surpasses the SOTA few-shot detector method FSOD by 21.08 MAE and 67.80 RMSE on validation set, 18.21 MAE and 55.11 RMSE on test set. We also excel the SOTA FSC method FamNet by 8.47 MAE and 21.87 RMSE on validation set, 7.76 MAE and 14.00 RMSE on test set. Note that FamNet needs test-time adaptation when used for novel classes, while *our SAFECOUNT needs no test-time adaptation at all*. These significant advantages demonstrate the effectiveness of our method. In Fig. 4, we show some qualitative results of SAFECOUNT. Compared with Famnet [26], our SAFECOUNT has much stronger ability to separate each independent object within densely packed objects, thus helps obtain an accurate

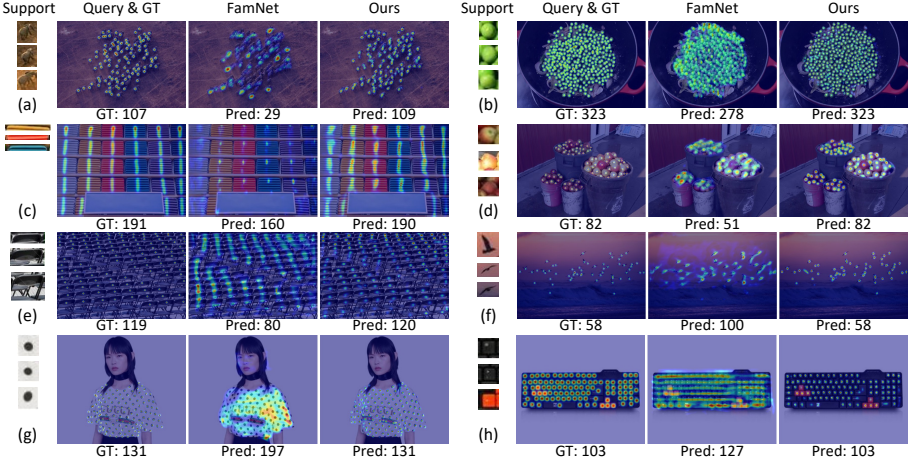


Fig. 4. Qualitative results on the FSC-147 dataset [26] under the 3-shot case. For each example, *from left to right*: support images, query image overlaid by the ground-truth density map, predicted density map by FamNet [26], and our prediction. The numbers below represent the counting results

count. Especially, for densely packed green peas (Fig. 4b), we not only exactly predict the object count, but also localize target objects with quite high precise that every single object could be clearly distinguished.

Subset Collected from COCO in FSC-147. In the validation set and test set of FSC-147, the images collected from COCO are also used as evaluation datasets, especially for the comparison with detection-based approaches since COCO is a popular detection benchmark. FSC-147 provides three COCO pre-trained detectors, including Faster-RCNN [28], RetinaNet [19], and Mask-RCNN [10]. Note that these detectors are pre-trained on COCO containing thousands of target objects, while FSC approach needs only 3 support images. Besides these baselines, Our approach is also compared with FSC approach FamNet [26]. Quantitative results are provided in Tab. 3b. Our approach surpasses COCO pre-trained Mask-RCNN with a quite large margin (29.66 MAE and 108.88 RMSE on validation set, 22.43 MAE and 56.32 RMSE on test set). Moreover, our method significantly outperforms FSC method FamNet by 16.97 MAE and 44.80 RMSE on validation set, 9.63 MAE and 22.24 RMSE on test set. This performance superiority proves the strong counting ability of our approach.

Cross-validation of FSC-147. The dataset split and shot number are both fixed in FSC-147 benchmark, which could not provide a comprehensive evaluation. Therefore, we incorporate FSC-147 with cross-validation to evaluate FSC methods with 4 dataset splits and 2 shot numbers. Our approach is compared with FSC baselines including GMN [23] and FamNet [26]. These baselines are trained and evaluated by ourselves with the official code. The cross-validation results are shown in Tab. 4, where fold- i ($i = 0, 1, 2, 3$) indicates the test set. Under all dataset splits and shot numbers, our method significantly excels baseline methods with both MAE and RMSE. Averagely, we outperform FamNet by 8.82 MAE

Table 3. Quantitative results on FSC-147 dataset [26], where we surpass other competitors by a sufficiently large margin. * and † respectively mark the few-shot detectors and COCO pre-trained detectors, whose performance are provided by the benchmark [26]. ‡ indicates the few-shot counting methods. Note that, unlike FamNet [26], our method does *not* require test-time adaptation for novel classes

(a) Evaluation on <i>full</i> FSC-147					(b) Evaluation on a subset of FSC-147, which is collected from COCO [20]				
Method	Val Set		Test Set		Method	Val-COCO		Test-COCO	
	MAE	RMSE	MAE	RMSE		MAE	RMSE	MAE	RMSE
* FR [13]	45.45	112.53	41.64	141.04	Faster-RCNN [28]	52.79	172.46	36.20	79.59
* FSOD [7]	36.36	115.00	32.53	140.65	† RetinaNet [19]	63.57	174.36	52.67	85.86
GMN [23]	29.66	89.81	26.52	124.57	Mask-RCNN [10]	52.51	172.21	35.56	80.00
‡ MAML [8]	25.54	79.44	24.90	112.68	FamNet [26]	39.82	108.13	22.76	45.92
‡ FamNet [26]	23.75	69.07	22.08	99.54	‡ Ours	22.85	63.33	13.13	23.68
Ours	15.28	47.20	14.32	85.54					

Table 4. Counting performance with cross-validation setting on FSC-147 dataset [26]. Fold- i ($i = 0, 1, 2, 3$) indicates the test set. Δ stands for the averaged improvement of the 3-shot case over the 1-shot case

Metric	Method	1-shot					3-shot					Δ
		Fold-0	Fold-1	Fold-2	Fold-3	Mean	Fold-0	Fold-1	Fold-2	Fold-3	Mean	
MAE	GMN [23]	37.44	21.89	31.52	32.73	30.90	36.53	21.43	31.23	31.51	30.18	-0.72
	FamNet [26]	27.98	15.75	21.32	22.33	21.85	26.32	15.51	21.28	21.96	21.27	-0.58
	Ours	17.64	6.97	12.96	14.55	13.03	13.21	6.58	12.43	14.16	11.60	-1.43
RMSE	GMN [23]	111.68	45.75	127.94	75.45	90.21	109.31	44.44	128.77	73.76	89.07	-1.14
	FamNet [26]	86.04	34.61	101.68	53.47	68.95	76.03	33.41	107.45	50.25	66.79	-2.16
	Ours	53.99	16.13	85.28	39.66	48.77	38.94	14.25	88.72	38.30	45.05	-3.72

and 20.18 RMSE in 1-shot case, 9.67 MAE and 21.74 RMSE in 3-shot case. Moreover, from 1-shot case to 3-shot case, our approach gains more performance improvement than two baseline methods, reflecting the superior ability of our SAFECOUNT to utilize multiple support images.

4.3 Class-specific Object Counting

Our approach is designed to be a general class-agnostic FSC approach, counting objects of novel classes with only a few support images. Nonetheless, we also train and evaluate our method on class-specific counting tasks to further testify its superiority. The training setup is detailed in Appendix A.

The **car counting benchmarks**: CARPK [12] and PUCPR+ [12], and **crowd counting benchmarks**: UCSD [3], Mall [4], and ShanghaiTech [51] are chosen to evaluate our method on class-specific counting tasks. For each dataset, 5 support images are randomly sampled from the training set and **fixed for both training and test**. As shown in Tab. 5, our method is compared with four kinds of competitors: *detectors*, *single-class crowd counting methods*, *multi-class counting methods*, and *FSC methods*. Note that *multi-class counting methods* could only count classes occurring in the training set, while *FSC methods*

Table 5. Counting performance on class-specific datasets, including CARPK [12], PUCPR+ [12], UCSD [3], Mall [4], and ShanghaiTech (Part A & Part B) [51]

(a) Car Counting					(b) Crowd Counting (MAE)					
Method	CARPK		PUCPR+		Method	UCSD	Mall	PartA	PartB	
	MAE	RMSE	MAE	RMSE						
1	YOLO [27]	48.89	57.55	156.00	200.42	Crowd CNN [49]	1.60	-	181.8	32.0
	F-RCNN [28]	47.45	57.39	111.40	149.35	MCNN [51]	1.07	-	110.2	26.4
	S-RPN [12]	24.32	37.62	39.88	47.67	Switch-CNN [2]	1.62	-	90.4	21.6
	RetinaNet [19]	16.62	22.30	24.58	33.12	2 CP-CNN [32]	-	-	73.6	20.1
	LPN [12]	23.80	36.79	22.76	34.46	CRSNet [18]	1.16	-	68.2	10.6
						RPNNet [47]	-	-	61.2	8.1
3	One Look [24]	59.46	66.84	21.88	36.73	GLF [37]	-	-	61.3	7.3
	IEP Count [34]	51.83	-	15.17	-	3 LC-FCN8 [15]	1.51	2.42	-	13.14
	PDEM [9]	6.77	8.52	7.16	12.00	LC-PSPNet [15]	1.01	2.00	-	21.61
4	GMN [23]	7.48	9.90	-	-	GMN [23]	-	-	95.8	-
	FamNet [26]	18.19	33.66	14.68 [†]	19.38 [†]	4 FamNet [26]	2.70 [†]	2.64 [†]	159.11 [†]	24.90 [†]
Ours					Ours	0.98	1.69	73.70	9.98	

¹ Detectors provided by the benchmark [12].

² Single-class crowd counting methods.

³ Multi-class counting methods (classes for training and test must be the same).

⁴ Few-shot counting methods. [†] trained and evaluated by ourselves with the official code.

can count unseen classes without any retraining. For car counting tasks, our approach surpasses all compared methods considerably. For UCSD and Mall where the crowd is relatively sparse, our approach outperforms all counterpart methods stably. The significant improvements verify the efficacy of our method. For ShanghaiTech, we outperform all *multi-class counting methods* and *FSC methods* with a large margin, and achieves competitive performance on par with *single-class crowd counting methods*. It is emphasized that, our method is not tailored to the specific crowd counting task, while the compared methods are.

4.4 Ablation Study

To verify the effectiveness of the proposed modules and the selection of hyper-parameters, we implement extensive ablation studies on FSC-147 [26].

SCM and FEM. To demonstrate the effectiveness of proposed SCM and FEM modules, we conduct diagnostic experiments respectively on similarity comparison and feature enhancement. The substitute of FEM is to concatenate the similarity map and query feature together, then recover the feature dimension through a 1×1 convolutional layer. To replace SCM, we remove our added normalization components including LN, EN, and SN, and adopt a 1×1 convolutional layer instead. The ablation results are shown in Tab. 6a. Both SCM and FEM are necessary and effective for our SAFECount. Specifically, when we replace FEM, the performance drops remarkably by 9.05 MAE in test set. This reflects that FEM is of vital significance in our SAFECount, since the core of our insight, *i.e.* feature enhancement, is completed in FEM. Besides, when we remove SCM, the performance also drops to a large extent by 3.35 MAE in test set. This indicates that SCM promotes the performance to a large degree, because SCM could derive a similarity map with a proper value range.

Table 6. Ablation studies on (a) the function of the proposed similarity comparison module (SCM) and feature enhancement module (FEM), (b) the score normalization used in SCM, (c) the stacked number of our proposed SAFECOUNT block, and (d) the place to perform density map regression

(a) SCM & FEM						(b) Score Normalization					
SCM	FEM	Val Set		Test Set		ENorm	SNorm	Val Set		Test Set	
		MAE	RMSE	MAE	RMSE			MAE	RMSE	MAE	RMSE
✓	✗	21.45	59.15	23.37	98.01	✗	✗	22.19	66.52	20.48	99.74
✗	✓	17.57	58.63	17.67	94.93	✓	✗	16.55	51.87	15.14	85.65
✓	✓	15.28	47.20	14.32	85.54	✗	✓	16.58	51.26	16.40	93.97
						✓	✓	15.28	47.20	14.32	85.54

(c) Block Number						(d) Similarity Map <i>v.s.</i> Enhanced Feature					
Block Number	Val Set		Test Set			Val Set		Test Set			
	MAE	RMSE	MAE	RMSE		MAE	RMSE	MAE	RMSE		
1	16.23	55.34	16.46	92.62							
2	16.04	54.53	15.36	87.35							
3	15.78	53.39	14.74	88.22							
4	15.28	47.20	14.32	85.54							
5	15.67	50.73	15.54	96.10							

		Val Set		Test Set	
		MAE	RMSE	MAE	RMSE
Raw Similarity		24.36	74.61	23.65	108.77
1-block Feature		16.23	55.34	16.46	92.62
4-block Similarity		19.74	64.30	18.70	99.34
4-block Feature		15.28	47.20	14.32	85.54

Score Normalization. To explore the effect of ENorm and SNorm, we conduct ablation experiments regarding these two normalization methods. The results are given in Tab. 6b. Even if without any score normalization, we still stably outperform all baselines in Tab. 3. This largely attributes to our SAFECOUNT architecture. Adding either ENorm or SNorm improves the performance greatly (≥ 4 MAE in test set), indicating the significance of score normalization. ENorm together with SNorm brings the best performance, reflecting that the two normalization methods could cooperate together for further performance improvement.

Block Number. It has been described in Sec. 3.3 that our SAFECOUNT could be formulated to a multi-block architecture. To explore the influence of the block number, we implement experiments with different block numbers. As shown in Tab. 6c, only 1-block SAFECOUNT has achieved state-of-the-art performance by a large margin, which illustrates the effectiveness of our designed SAFECOUNT architecture. Furthermore, the performance gets improved gradually when the block number increases from 1 to 4, and decreased slightly when the block number is added to 5. As proven in [11], too many blocks could hinder the training process, decreasing the performance. Finally, we set the block number as 4 for FSC-147.

Regressing from Similarity Map *v.s.* Enhanced Feature. The density map could be regressed from either the enhanced feature or the similarity map. We conduct experiments to compare these two choices. The results are provided in Tab. 6d. *Raw Similarity* is similar to FamNet [26] but without the test-time adaptation, predicting the density map directly from the raw similarity. The rest 3 methods follow our designed architecture, where *i*-block *Similarity* and *i*-block *Feature* mean that the density map is regressed from the similarity map and enhanced feature of the i^{th} block, respectively. It is obvious that *1-block Feature* and *4-block Feature* significantly outperform *Raw Similarity* and *4-block Similarity*, respectively. The reason might be that the enhanced feature contains

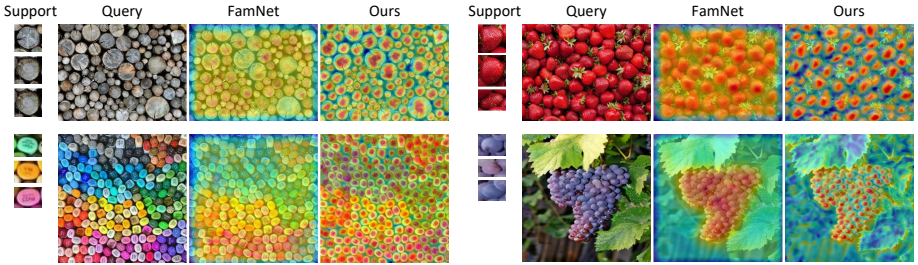


Fig. 5. Visualization of the similarity maps developed by FamNet [26] and our SAFECOUNT. Benefiting from the proposed SAFECOUNT block, our approach recognizes *much clearer boundaries* between densely packed objects

much richer semantics than the similarity map and could filter out some erroneous high similarity values, *i.e.* the high similarity values that do not correspond to target objects, as proven in stereo matching literature [36].

4.5 Visualization

We visualize and compare the intermediate similarity map in FamNet [26] and our SAFECOUNT in Fig. 5, which could intuitively explain why SAFECOUNT outperforms FamNet by such a large margin. Here the similarity map in SAFECOUNT means the one in the last block. In FamNet, the similarity map is derived by direct comparison between the raw features of the query image and support images. However, the similarity map is far less informative than features, making it hard to identify clear boundaries within densely packed objects. In contrast, we weigh the support feature based on the similarity values, then integrate the similarity-weighted feature into the query feature. This design encodes the support-query relationship into features, while keeping the rich semantics extracted from the image. Also, our similarity comparison module (SCM) is learnable. Benefiting from these, our SAFECOUNT gets very clear boundaries between densely packed objects in the similarity map, which is beneficial to regress an accurate count.

5 Conclusion

In this work, to tackle the challenging few-shot object counting task, we propose the similarity-aware feature enhancement block, dubbed as SAFECOUNT, composed of a similarity comparison module (SCM) and a feature enhancement module (FEM). Our SCM compares the support feature and the query feature to derive a score map. Then the score map is normalized across both the exemplar dimension and the spatial dimensions, producing a reliable similarity map. The FEM views these similarity values as weighting coefficients to integrate the support features into the query feature. By doing so, the model would pay more attention to the regions similar to support images, bringing distinguishable borders within densely packed objects. Extensive experiments on various benchmarks and training settings demonstrate that our SAFECOUNT achieves state-of-the-art performance by a considerably large margin.

References

1. Arteta, C., Lempitsky, V., Zisserman, A.: Counting in the wild. In: Eur. Conf. Comput. Vis. pp. 483–498 (2016)
2. Babu Sam, D., Surya, S., Venkatesh Babu, R.: Switching convolutional neural network for crowd counting. In: IEEE Conf. Comput. Vis. Pattern Recog. pp. 5744–5752 (2017)
3. Chan, A.B., Liang, Z.S.J., Vasconcelos, N.: Privacy preserving crowd monitoring: Counting people without people models or tracking. In: IEEE Conf. Comput. Vis. Pattern Recog. pp. 1–7 (2008)
4. Chen, K., Loy, C.C., Gong, S., Xiang, T.: Feature mining for localised crowd counting. In: Brit. Mach. Vis. Conf. p. 3 (2012)
5. Deng, J., Dong, W., Socher, R., Li, L.J., Li, K., Fei-Fei, L.: Imagenet: A large-scale hierarchical image database. In: IEEE Conf. Comput. Vis. Pattern Recog. pp. 248–255 (2009)
6. Fan, Q., Zhuo, W., Tang, C.K., Tai, Y.W.: Few-shot object detection with attention-rpn and multi-relation detector. In: IEEE Conf. Comput. Vis. Pattern Recog. pp. 4013–4022 (2020)
7. Fan, Q., Zhuo, W., Tang, C.K., Tai, Y.W.: Few-shot object detection with attention-rpn and multi-relation detector. In: IEEE Conf. Comput. Vis. Pattern Recog. pp. 4013–4022 (2020)
8. Finn, C., Abbeel, P., Levine, S.: Model-agnostic meta-learning for fast adaptation of deep networks. In: Int. Conf. Mach. Learn. pp. 1126–1135 (2017)
9. Goldman, E., Herzig, R., Eisenschtat, A., Goldberger, J., Hassner, T.: Precise detection in densely packed scenes. In: IEEE Conf. Comput. Vis. Pattern Recog. pp. 5227–5236 (2019)
10. He, K., Gkioxari, G., Dollár, P., Girshick, R.: Mask R-CNN. In: Int. Conf. Comput. Vis. pp. 2961–2969 (2017)
11. He, K., Zhang, X., Ren, S., Sun, J.: Deep residual learning for image recognition. In: IEEE Conf. Comput. Vis. Pattern Recog. pp. 770–778 (2016)
12. Hsieh, M.R., Lin, Y.L., Hsu, W.H.: Drone-based object counting by spatially regularized regional proposal network. In: Int. Conf. Comput. Vis. pp. 4145–4153 (2017)
13. Kang, B., Liu, Z., Wang, X., Yu, F., Feng, J., Darrell, T.: Few-shot object detection via feature reweighting. In: Int. Conf. Comput. Vis. pp. 8420–8429 (2019)
14. Kingma, D.P., Ba, J.: Adam: A method for stochastic optimization. arXiv preprint arXiv:1412.6980 (2014)
15. Laradji, I.H., Rostamzadeh, N., Pinheiro, P.O., Vazquez, D., Schmidt, M.: Where are the blobs: Counting by localization with point supervision. In: Eur. Conf. Comput. Vis. pp. 547–562 (2018)
16. Leibe, B., Seemann, E., Schiele, B.: Pedestrian detection in crowded scenes. In: IEEE Conf. Comput. Vis. Pattern Recog. pp. 878–885 (2005)
17. Lempitsky, V., Zisserman, A.: Learning to count objects in images. In: Adv. Neural Inform. Process. Syst. pp. 1324–1332 (2010)
18. Li, Y., Zhang, X., Chen, D.: Csrnet: Dilated convolutional neural networks for understanding the highly congested scenes. In: IEEE Conf. Comput. Vis. Pattern Recog. pp. 1091–1100 (2018)
19. Lin, T.Y., Goyal, P., Girshick, R., He, K., Dollár, P.: Focal loss for dense object detection. In: Int. Conf. Comput. Vis. pp. 2980–2988 (2017)

20. Lin, T.Y., Maire, M., Belongie, S., Hays, J., Perona, P., Ramanan, D., Dollár, P., Zitnick, C.L.: Microsoft COCO: Common objects in context. In: *Eur. Conf. Comput. Vis.* pp. 740–755 (2014)
21. Liu, J., Gao, C., Meng, D., Hauptmann, A.G.: DecideNet: Counting varying density crowds through attention guided detection and density estimation. In: *IEEE Conf. Comput. Vis. Pattern Recog.* pp. 5197–5206 (2018)
22. Liu, L., Chen, J., Wu, H., Li, G., Li, C., Lin, L.: Cross-modal collaborative representation learning and a large-scale rgbt benchmark for crowd counting. In: *IEEE Conf. Comput. Vis. Pattern Recog.* pp. 4823–4833 (2021)
23. Lu, E., Xie, W., Zisserman, A.: Class-agnostic counting. In: *Asian Conf. Comput. Vis.* pp. 669–684 (2018)
24. Mundhenk, T.N., Konjevod, G., Sakla, W.A., Boakye, K.: A large contextual dataset for classification, detection and counting of cars with deep learning. In: *Eur. Conf. Comput. Vis.* pp. 785–800 (2016)
25. Ranjan, V., Le, H., Hoai, M.: Iterative crowd counting. In: *Eur. Conf. Comput. Vis.* pp. 270–285 (2018)
26. Ranjan, V., Sharma, U., Nguyen, T., Hoai, M.: Learning to count everything. In: *IEEE Conf. Comput. Vis. Pattern Recog.* pp. 3394–3403 (2021)
27. Redmon, J., Divvala, S., Girshick, R., Farhadi, A.: You only look once: Unified, real-time object detection. In: *IEEE Conf. Comput. Vis. Pattern Recog.* pp. 779–788 (2016)
28. Ren, S., He, K., Girshick, R., Sun, J.: Faster R-CNN: Towards real-time object detection with region proposal networks. In: *Adv. Neural Inform. Process. Syst.* pp. 91–99 (2015)
29. Sam, D.B., Babu, R.V.: Top-down feedback for crowd counting convolutional neural network. In: *Assoc. Adv. Artif. Intell.* (2018)
30. Shi, Z., Zhang, L., Liu, Y., Cao, X., Ye, Y., Cheng, M.M., Zheng, G.: Crowd counting with deep negative correlation learning. In: *IEEE Conf. Comput. Vis. Pattern Recog.* pp. 5382–5390 (2018)
31. Sindagi, V.A., Patel, V.M.: Generating high-quality crowd density maps using contextual pyramid cnns. In: *Int. Conf. Comput. Vis.* pp. 1861–1870 (2017)
32. Sindagi, V.A., Patel, V.M.: Generating high-quality crowd density maps using contextual pyramid cnns. In: *Int. Conf. Comput. Vis.* pp. 1861–1870 (2017)
33. Song, Q., Wang, C., Jiang, Z., Wang, Y., Tai, Y., Wang, C., Li, J., Huang, F., Wu, Y.: Rethinking counting and localization in crowds: A purely point-based framework. In: *Int. Conf. Comput. Vis.* pp. 3365–3374 (2021)
34. Stahl, T., Pintea, S.L., Van Gemert, J.C.: Divide and count: Generic object counting by image divisions. *IEEE Trans. Image Process.* pp. 1035–1044 (2019)
35. Stewart, R., Andriluka, M., Ng, A.Y.: End-to-end people detection in crowded scenes. In: *IEEE Conf. Comput. Vis. Pattern Recog.* pp. 2325–2333 (2016)
36. Sun, D., Yang, X., Liu, M.Y., Kautz, J.: Pwc-net: Cnns for optical flow using pyramid, warping, and cost volume. In: *IEEE Conf. Comput. Vis. Pattern Recog.* pp. 8934–8943 (2018)
37. Wan, J., Liu, Z., Chan, A.B.: A generalized loss function for crowd counting and localization. In: *IEEE Conf. Comput. Vis. Pattern Recog.* pp. 1974–1983 (2021)
38. Wan, J., Luo, W., Wu, B., Chan, A.B., Liu, W.: Residual regression with semantic prior for crowd counting. In: *IEEE Conf. Comput. Vis. Pattern Recog.* pp. 4036–4045 (2019)
39. Wang, M., Wang, X.: Automatic adaptation of a generic pedestrian detector to a specific traffic scene. In: *IEEE Conf. Comput. Vis. Pattern Recog.* pp. 3401–3408 (2011)

40. Wang, Z., Bovik, A.C., Sheikh, H.R., Simoncelli, E.P.: Image quality assessment: from error visibility to structural similarity. *IEEE Trans. Image Process.* pp. 600–612 (2004)
41. Wertheimer, D., Tang, L., Hariharan, B.: Few-shot classification with feature map reconstruction networks. In: *IEEE Conf. Comput. Vis. Pattern Recog.* pp. 8012–8021 (2021)
42. Wu, J., Liu, S., Huang, D., Wang, Y.: Multi-scale positive sample refinement for few-shot object detection. In: *Eur. Conf. Comput. Vis.* pp. 456–472 (2020)
43. Xiong, F., Shi, X., Yeung, D.Y.: Spatiotemporal modeling for crowd counting in videos. In: *Int. Conf. Comput. Vis.* pp. 5151–5159 (2017)
44. Yan, Z., Yuan, Y., Zuo, W., Tan, X., Wang, Y., Wen, S., Ding, E.: Perspective-guided convolution networks for crowd counting. In: *Int. Conf. Comput. Vis.* pp. 952–961 (2019)
45. Yang, L., Zhuo, W., Qi, L., Shi, Y., Gao, Y.: Mining latent classes for few-shot segmentation. In: *Int. Conf. Comput. Vis.* pp. 8721–8730 (2021)
46. Yang, S.D., Su, H.T., Hsu, W.H., Chen, W.C.: Class-agnostic few-shot object counting. In: *IEEE Winter Conf. Appl. Comput. Vis.* pp. 870–878 (2021)
47. Yang, Y., Li, G., Wu, Z., Su, L., Huang, Q., Sebe, N.: Reverse perspective network for perspective-aware object counting. In: *IEEE Conf. Comput. Vis. Pattern Recog.* pp. 4374–4383 (2020)
48. Zhang, C., Lin, G., Liu, F., Yao, R., Shen, C.: CANet: Class-agnostic segmentation networks with iterative refinement and attentive few-shot learning. In: *IEEE Conf. Comput. Vis. Pattern Recog.* pp. 5217–5226 (2019)
49. Zhang, C., Li, H., Wang, X., Yang, X.: Cross-scene crowd counting via deep convolutional neural networks. In: *IEEE Conf. Comput. Vis. Pattern Recog.* pp. 833–841 (2015)
50. Zhang, Q., Lin, W., Chan, A.B.: Cross-view cross-scene multi-view crowd counting. In: *IEEE Conf. Comput. Vis. Pattern Recog.* pp. 557–567 (2021)
51. Zhang, Y., Zhou, D., Chen, S., Gao, S., Ma, Y.: Single-image crowd counting via multi-column convolutional neural network. In: *IEEE Conf. Comput. Vis. Pattern Recog.* pp. 589–597 (2016)

Appendix

A Network Architecture and Training Configurations

Feature Extractor. We select ResNet-18 [11] pre-trained on ImageNet [5] as the feature extractor.¹ Given a query image, $Q \in \mathbb{R}^{3 \times 512 \times 512}$, we resize the outputs of the first three residual stages of ResNet-18 to the same size, 128×128 , and concatenate them along the channel dimension. Afterward, a 1×1 convolutional layer is applied to reduce the channel dimension to 256, resulting in the query feature, $\mathbf{f}_Q \in \mathbb{R}^{256 \times 128 \times 128}$. The size of ROI pooling [28] is set as 3×3 , so the support feature, \mathbf{f}_S , has the shape of $K \times 256 \times 3 \times 3$ in the K -shot case. The backbone is frozen during training, while the 1×1 convolutional layer is not.

Similarity Comparison Module (SCM). Our SCM is implemented with three steps: *learnable feature projection*, *feature comparison*, and *score normalization*.

¹ We borrow the checkpoint [here](#).

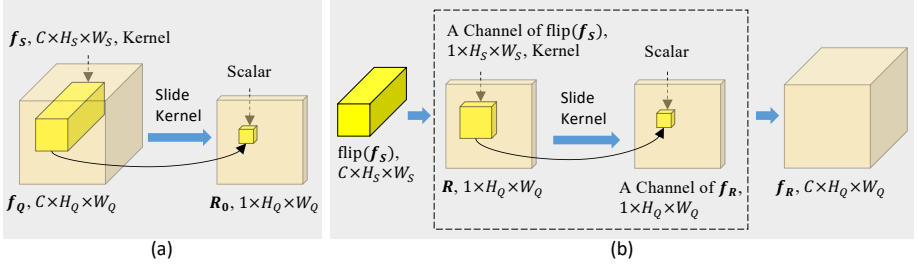


Fig. 6. (a) Illustration of the *feature comparison* in SCM under the 1-shot case, where the feature projection is omitted. (b) Illustration of the *weighted feature aggregation* in FEM under the 1-shot case

The *feature comparison* is implemented by convoluting the query feature, f_Q , with the support feature, f_S , as kernels, deriving a score map, R_0 . This process is illustrated intuitively in Fig. 6a. Other components in SCM have been detailed in the paper. The SCM finally outputs a similarity map, $R \in \mathbb{R}^{K \times 1 \times 128 \times 128}$.

Feature Enhancement Module (FEM).

The FEM is composed of two steps: *weighted feature aggregation* and *learnable feature fusion*. The *weighted feature aggregation* treats the values in the similarity map, R , as weighting coefficients to integrate f_S , producing the similarity-weighted feature, f_R . This process is realized by the convolution, as shown in Fig. 6b. Besides, before serving as the convolutional kernels, f_S is flipped both horizontally and vertically. As illustrated in Fig. 7, the flipping helps f_R inherit the spatial structure from f_S . In Fig. 7, R

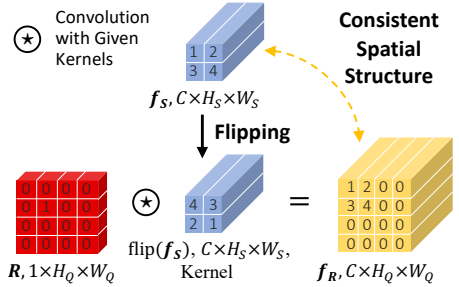


Fig. 7. Illustration of kernel flipping in FEM, which helps f_R inherit the spatial structure from f_S

is a unit impulse function, meaning that only one position has the maximum similarity with f_S , while other positions have no similarity with f_S at all. Therefore, f_R should have a sub-part exactly the same with f_S in the position corresponding to the maximum similarity, while the others should be zero vectors. The *weighted feature aggregation* constructs f_R following the above insights via flipping and convolution. The *learnable feature fusion* is completed by a 2-layer convolutional network, skip connection, and layer normalization. The architecture of the convolutional network is shown in Tab. 7a. Other components in FEM have been detailed in the paper. Eventually, the FEM produces the enhanced feature, $f'_Q \in \mathbb{R}^{256 \times 128 \times 128}$.

Regress Head. The regress head regresses the density map, $D \in \mathbb{R}^{512 \times 512}$, from the enhanced feature, f'_Q . The regression head is composed of a sequence of convolutional layers, followed by the Leaky ReLU activation and bi-linear upsampling, as shown in Tab. 7b.

Table 7. Network architectures of (a) the *learnable feature fusion* in FEM, and (b) the regress head

(a) Architecture of the <i>learnable feature fusion</i> in FEM, where the skip connection and the layer normalization are omitted					(b) Architecture of the regress head				
layer	kernel	in	out	activation	layer	kernel	in	out	activation followed by
Conv	1×1	256	1024	Leaky ReLU	Conv	3×3	256	64	Leaky ReLU $2 \times$ Upsample
Conv	1×1	1024	256	-	Conv	3×3	64	32	Leaky ReLU $2 \times$ Upsample
					Conv	1×1	32	1	Leaky ReLU -

Multi-block Architecture. The enhanced feature derived by one block, f'_Q , could serve as the input to the next block by taking the place of the query feature, f_Q , forming a multi-block architecture. As for another input of the next block, the support feature, f_S , there are two choices. If the support image is cropped from the query image, f_S is updated by ROI pooling on newly obtained f'_Q . If not, f_S does not change in different blocks.

Training Configuration on FSC-147 [26]. The sizes of the query image, the query feature, and the support feature are selected as 512×512 , 128×128 , and 3×3 , respectively. The block number is set as 4. The model is trained with Adam optimizer [14] for 200 epochs with batch size 8. The hyper-parameter ϵ in Adam optimizer is set as $4e-11$, much smaller than the default $1e-8$, considering the small norm of the loss and the gradient. The learning rate is set as $2e-5$ initially, and it is dropped by 0.25 after every 80 epochs. Data augmentation methods including random horizontal flip, color jitter, and random gamma transformation are adopted.

Training Configuration on Class-specific Counting Datasets. The size of the support feature is set as 1×1 . The block number is set as 2. Data augmentation methods including random flip, color jitter, random rotation, and random grayscale are used to prevent over-fitting and improve the generalization ability. Other setups are the same as **FSC-147**.

B Ablation Studies

Loss Function. The loss function described in the paper is MSE loss. Actually, we also implement experiments with another SSIM term as follows,

$$\mathcal{L} = \text{MSE}(D, D_{GT}) - \alpha \text{SSIM}(D, D_{GT}), \quad (10)$$

where $\text{SSIM}(\cdot)$ is the structural similarity function [40], which measures the local pattern consistence between the predicted density map and the ground-truth, α is the weight term. The results with different α are shown in Tab. 8a. Adding the SSIM term promotes the performance of MAE but with the sacrifice of RMSE. Compared with MAE, RMSE relies more heavily on the prediction of the samples with extremely large count. Therefore, we speculate that the SSIM term is beneficial to some samples, but may harm the samples with extremely large count. We finally decide not to add the SSIM term, because the performance drop of RMSE is too large.

Table 8. Ablation studies regarding (a) loss weight term α in Eq. (10), (b) size of ROI pooling, (c) kernel flipping in FEM, and (d) training or freezing backbone

(a) α in Eq. (10)					(b) Size of ROI Pooling				
α	Val Set		Test Set		Size of ROI Pooling	Val Set		Test Set	
	MAE	RMSE	MAE	RMSE		MAE	RMSE	MAE	RMSE
1e-3	15.15	52.02	15.42	95.77	1×1	15.83	54.65	16.13	95.52
1e-4	14.18	53.65	13.55	89.69	3×3	15.28	47.20	14.32	85.54
1e-5	15.11	56.05	14.63	93.41	5×5	15.57	53.79	15.18	89.32
0	15.28	47.20	14.32	85.54					
(c) Kernel Flipping in FEM					(d) Training <i>v.s.</i> Freezing Backbone				
Flipping	Val Set		Test Set		Backbone	Val Set		Test Set	
	MAE	RMSE	MAE	RMSE		MAE	RMSE	MAE	RMSE
\times	16.78	57.47	15.35	93.59	Trained by lr	25.24	65.23	26.00	103.83
\checkmark	15.28	47.20	14.32	85.54	Trained by 0.1 \times lr	23.50	53.45	23.67	92.38
					Frozen	15.28	47.20	14.32	85.54

Size of ROI Pooling. To study the influence of the ROI pooling size, we conduct experiments with different ROI pooling sizes. The results are shown in Tab. 8b. The performance is the worst with the ROI pooling size as 1×1 , *i.e.* pooling to a support vector, since pooling to a support vector fully omits the spatial information of the support image. Adding the ROI pooling size to 3×3 brings stable improvement. However, further increasing the ROI pooling size to 5×5 decreases the performance slightly. This may be because too large ROI pooling size would slightly hinder the accurate localization of target objects. Accordingly, we select the ROI pooling size as 3×3 for FSC-147.

Kernel Flipping in FEM. As described in Appendix A, kernel flipping in FEM could help the similarity-weighted feature, \mathbf{f}_R , inherit the spatial structure from the support feature, \mathbf{f}_S . The effectiveness of adding the flipping is proven by ablation experiments, whose results are given in Tab. 8c. Adding the flipping could improve the performance stably (≥ 1 MAE), reflecting that preserving the spatial structure of \mathbf{f}_R benefits the counting performance.

Freezing Backbone. To explore the influence of training or fixing backbone, we conduct the ablation study on FSC-147 and the results are provided in Tab. 8d. When the backbone is trained with the same learning rate as other modules, the performance is worse. The performance is improved stably with the learning rate of the backbone reduced to 0.1 \times of other modules. Further, the performance achieves the best with a fully frozen backbone. This largely attributes to the class domain gap. In FSC-147, the classes in the validation set and the test set are different from those in the training set. Therefore, training backbone encourages the backbone to extract features that are more relevant to training classes, which decreases the performance in the validation set and the test set.

C More Results

Quantitative Results on Crowd Counting. The crowd counting results provided in the paper are only evaluated by MAE because of the page limit. Here we provide the results regarding both MAE and RMSE in Tab. 9.

Table 9. Quantitative results on crowd counting

Dataset	MAE	RMSE
UCSD [3]	0.98	1.27
Mall [4]	1.69	2.15
ShanghaiTech PartA [51]	73.70	118.76
ShanghaiTech PartB [51]	9.98	16.17

Qualitative Results on FSC-147 [26]. The qualitative results of FSC-147 are shown in Fig. 8, Fig. 9, and Fig. 10a. For each class, the images from top to down are the query image and the predicted density map. The objects circled by the red rectangles are the support images. The texts below the density map describe the counting results. Our SAFECOUNT could successfully count objects of all categories with various densities and scales, demonstrating strong generalization ability and robustness. Specifically, for both objects with extremely high density (*e.g.*, Legos in Fig. 9) and objects with quite sparse density (*e.g.*, Prawn Crackers in Fig. 9), both small objects (*e.g.*, Birds in Fig. 8) and large objects (*e.g.*, Horses in Fig. 8), both round objects (*e.g.*, Apples in Fig. 8) and square objects (*e.g.*, Stamps in Fig. 9), both vertical strip objects (*e.g.*, Skis in Fig. 9) and horizontal strip objects (*e.g.*, Shirts in Fig. 9), our approach could precisely count objects of interest with high localization accuracy.

Qualitative Results on Class-specific Object Counting. Our method is evaluated on two car counting datasets and three crowd counting datasets. For each dataset, five support images are randomly sampled from the training set and fixed for both training and test, as shown in Fig. 10b. The qualitative results on CARPK [12], PUCPR+ [12], UCSD [3], Mall [4], and ShanghaiTech [51] are shown in Fig. 10c-h. (1) *Car Counting*: Our approach could localize and count cars with different angles and scales successfully. Especially, in the cases that some cars are in the deep shadows (*e.g.*, the 7th, 11th examples in Fig. 10c, the 11st example in Fig. 10d) or partly hidden under the trees (*e.g.*, the 3rd, 10th examples in Fig. 10c, the 5th, 12nd examples in Fig. 10d), our method still accurately localizes these cars, indicating the superiority of our approach. (2) *Crowd Counting*: In the cases of UCSD and Mall where the crowd density is relatively sparse, our approach could count the number of persons precisely with extremely small error. For ShanghaiTech PartA, if the persons in the crowd are distinguishable (*e.g.*, the 1st, 11th examples in Fig. 10g), our model could localize each person precisely. If the persons are too crowded to distinguish (*e.g.*, the 2nd, 5th examples in Fig. 10g), our method could predict an accurate density estimate for crowds. For ShanghaiTech PartB where most persons are distinguishable, our approach successfully localizes and counts persons, indicating that our approach is capable of crowd counting with various crowd densities.



Fig. 8. Qualitative results on unseen classes in FSC-147 (from Ants to Keyboard Keys). There are only 2 images of Flowers in FSC-147

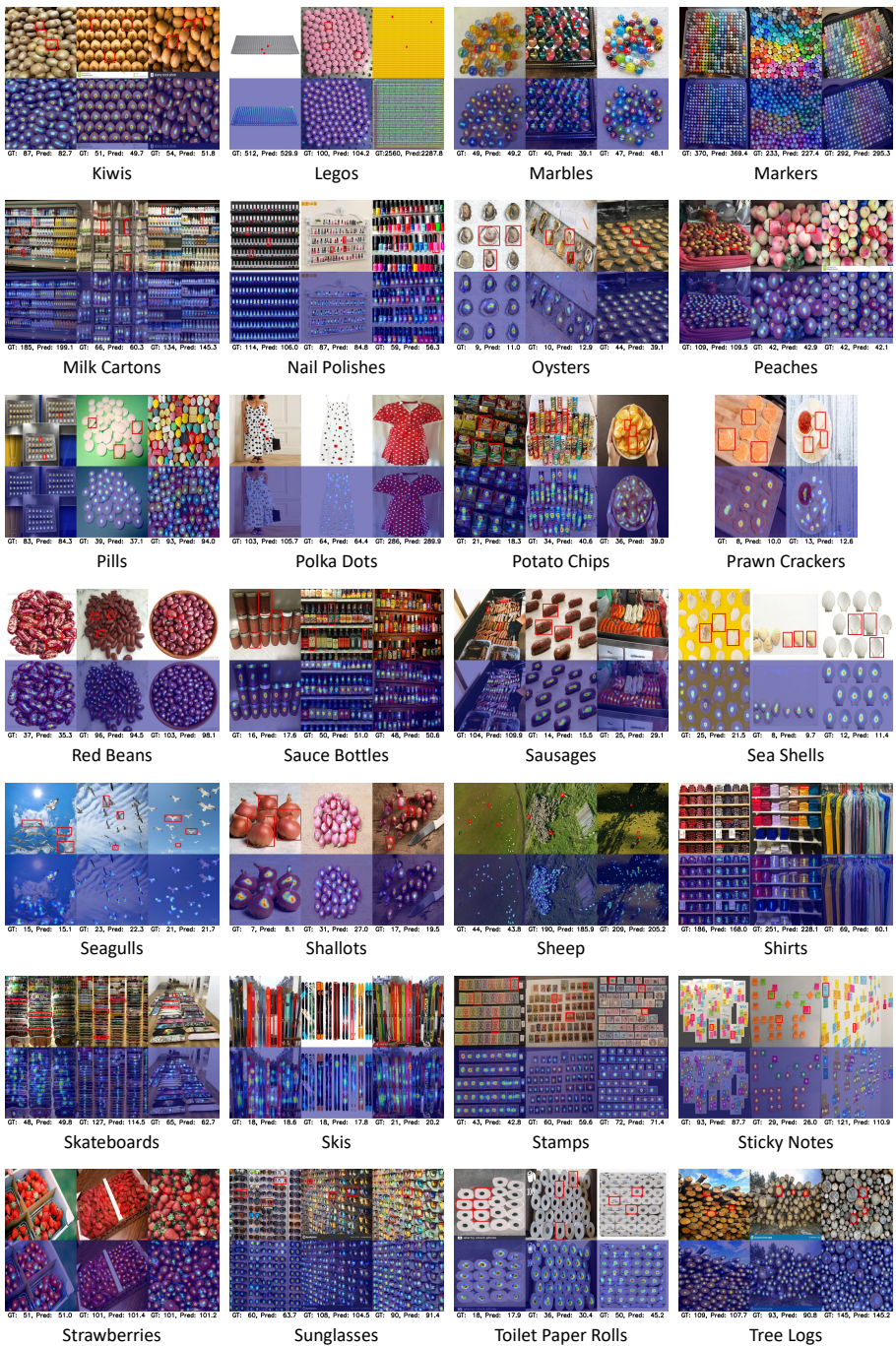


Fig. 9. Qualitative results on unseen classes in FSC-147 (from Kiwis to Tree Logs). There are only 2 images of Prawn Crackers in FSC-147

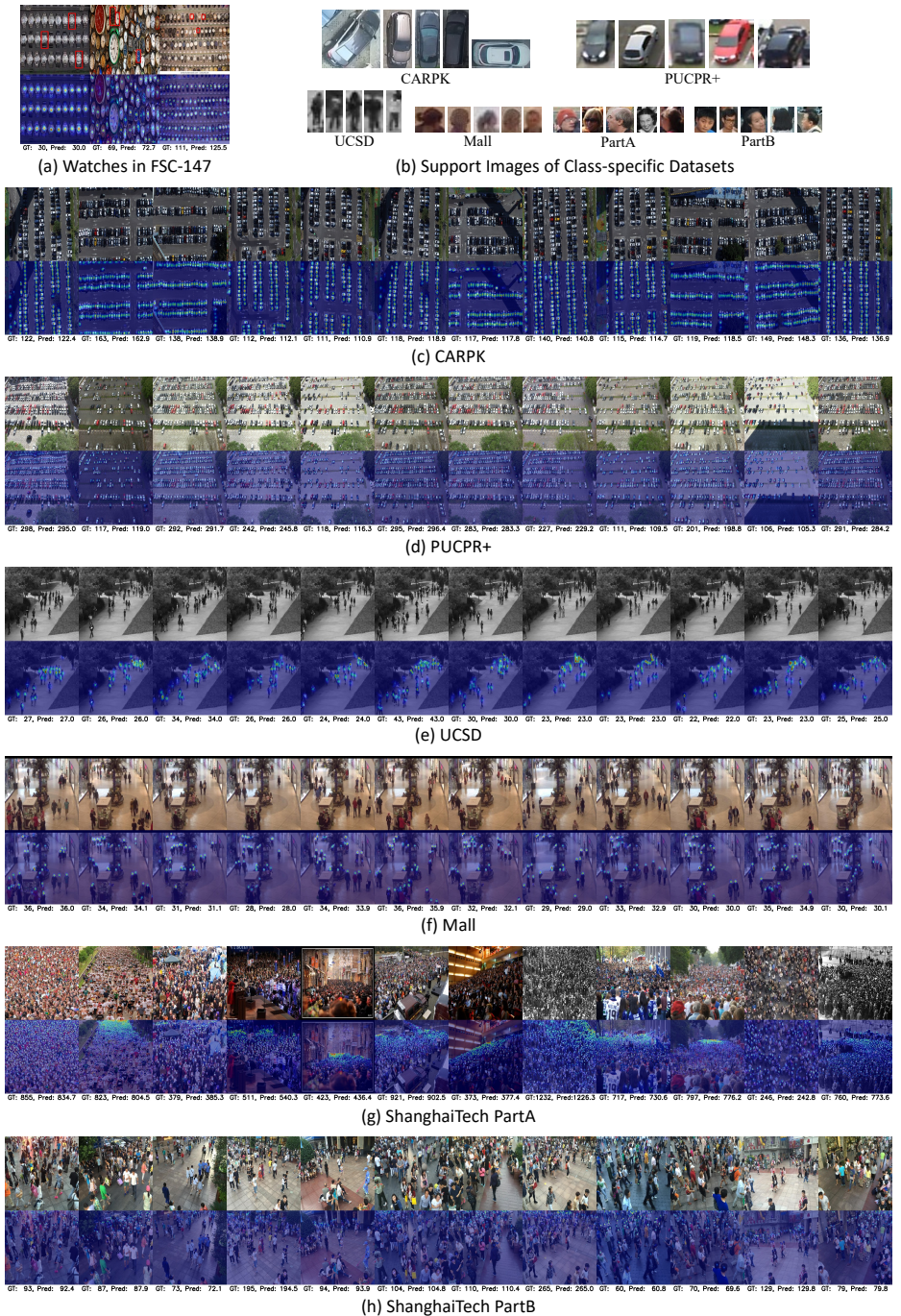


Fig. 10. (a) Qualitative results on unseen classes (Watches) in FSC-147. (b) Support images of class-specific datasets. (c-h) Qualitative results on class-specific datasets